J. Fluid Mech. (2012), *vol.* 691, *pp.* 315–340. © Cambridge University Press 2011
doi:10.1017/jfm.2011.477

Surface instability of an encapsulated bubble induced by an ultrasonic pressure wave

Yunqiao Liu[1]†, Kazuyasu Sugiyama[1], Shu Takagi[1,2] and Yoichiro Matsumoto[1]

[1] Department of Mechanical Engineering, School of Engineering, The University of Tokyo, 7-3-1 Hongo, Bunkyo-ku, Tokyo 113-8656, Japan

[2] Organ and Body Scale Team, CSRP, Riken, 2-1, Hirosawa, Wako-shi, Saitama 351-0198, Japan

(Received 26 January 2011; revised 30 July 2011; accepted 25 October 2011; first published online 6 December 2011)

In this paper, we investigate the shape stability of a nearly spherical bubble encapsulated by a viscoelastic membrane in an ultrasound field. To describe the dynamic balance on the bubble surface, the in-plane stress and the bending moment are incorporated into the governing equations for the perturbed radial flow of viscous incompressible fluid (Prosperetti, *Q. Appl. Math.*, vol. 34, 1977, p. 339). The radial motion of the bubble is obtained by solving the Rayleigh–Plesset equation with elastic stress. The deflection therefrom is linearized and expanded with respect to the Legendre polynomial of order $k \geqslant 2$. Two amplitudes for each shape mode are introduced because the membrane moves not only in the radial direction but also in the tangential direction. The system with a boundary layer approximation is reduced to Mathieu's equation. A simple expression for the natural frequency of the shape mode is derived, which is validated by direct numerical simulation. Stability diagrams for the higher-order shape mode are mapped out in the phase space of driving amplitude and frequency over a range of values of the elastic modulus of the membrane. The most unstable driving frequency is found to satisfy an integer multiple relationship of the form $2\omega_k/\omega_d = n$, due to the structure of Mathieu's equation in the system. In addition to the resonance interaction, liquid viscosity plays an important role in the stability of the encapsulated bubble.

Key words: bubble dynamics, membranes, parametric instability

1. Introduction

Encapsulated bubbles are widely used in medical ultrasound applications, e.g. ultrasound contrast agents (Lindner 2004) and drug delivery systems (Unger *et al.* 2001). The dynamic behaviour of the encapsulating membrane exposed in an ultrasound field is of importance in the applications of contrast-enhanced agents and drug-carrier capsules.

The dynamics of an encapsulated bubble is an extension of traditional bubble dynamics. Early studies incorporated linear membrane models into the standard Rayleigh–Plesset equation (de Jong, Cornet & Lancée 1994; Church 1995; Hoff, Sontum & Hovem 2000; Sarkar *et al.* 2005). Sarkar *et al.* (2005) found that

---

† Email address for correspondence: yqliu@fel.t.u-tokyo.ac.jp

elastic stress was overestimated when they compared their experimental measurements with the solutions of the linear models. Accordingly, a nonlinear constitutive law is needed to describe the realistic behaviour of the membrane. Marmottant *et al.* (2005) introduced an effective surface tension, which characterizes the buckled state, elastic expansion, and break-up. This model is validated by experimental measurements (see also Stride 2008; Overvelde *et al.* 2010). Tsiglifis & Pelekasis (2008) employed hyperelastic constitutive laws, which are defined by an energy function to relate finite strain to the stress, to describe the nonlinear dilatational elasticity. Nevertheless, the analysis was limited to radial dynamics.

For an encapsulated bubble in an ultrasound field, the shape instability is particularly important. The deformation induced by the ultrasonic pressure wave may lead to the break-up of a bubble, and thereby shorten the residence time of contrast agents or facilitate the drug release from carrier capsules. It is of primary importance to first perform a parameter study to determine whether the system is intrinsically stable or not. Therefore, we perform a linear analysis of the shape instability of an encapsulated bubble. This instability has been demonstrated experimentally: for example, Chomas *et al.* (2000), through optical imaging, suggested that the onset of fragmentation of contrast agent is directly linked to the loss of spherical symmetry. Their recorded wall velocity and acceleration provided strong evidence that the mechanism responsible for the fragmentation is the Rayleigh–Taylor instability. Postema *et al.* (2004) found that the number of fragments is determined by the dominant spherical harmonics oscillation mode. A systematic study of the non-spherical oscillations was carried out by Dollet *et al.* (2008). They concluded that the non-spherical deformation is a parametric instability driven by radial oscillation, requiring a finite time to grow and developing preferentially at the resonance radius of the radial oscillation.

Although the above experimental studies revealed complicated behaviour of an encapsulated bubble, they imply that the mechanism of the surface instability is similar to that of a gas bubble, which has been well studied: see Feng & Leal (1997), Plesset & Prosperetti (1977) and Brenner, Hilgenfeldt & Lohse (2002). In landmark work, Plesset (1954) introduced a small perturbation to the spherical interface and derived a differential equation for the amplitude a_k at the kth-order perturbation, which is widely referred to below:

$$\ddot{a}_k + 3\frac{\dot{R}}{R}\dot{a}_k + (k-1)\left[-\frac{\ddot{R}}{R} + (k+1)(k+2)\frac{\gamma}{\rho R^3}\right]a_k = 0, \tag{1.1}$$

where R is the instant radius, ρ the density of external liquid and γ the surface tension. From this equation, the natural frequency of the kth-order mode is easily obtained as

$$\omega_k^{gas} = \sqrt{(k-1)(k+1)(k+2)\frac{\gamma}{\rho R_0^2}}, \tag{1.2}$$

where R_0 is the initial radius. This formula of the natural frequency of the shape mode is the same as that presented by Lamb (1932). The differential equation (1.1) can be reduced to Mathieu's equation (Benjamin 1964). Based on the theory of Mathieu's equation, instability occurs when the higher-order and zeroth-order natural frequencies have an integer multiple relationship, i.e. $2\omega_k/\omega_0 = n$. The most unstable modes, namely one–two and one–one resonances when n is chosen as 1 and 2 respectively, were investigated by Feng & Leal (1993) and Yang, Feng & Leal (1993) from the perspective of energy transfer. The derived condition of instability was validated by Versluis *et al.* (2010) through a direct observation of the shape modes. These studies stressed that the resonance interaction between radial and shape modes is the key to induce surface instability.

The extension of the results for a gas bubble to an encapsulated bubble is not trivial. First, in order to describe the non-spherical deformation, a force balance in the normal direction is insufficient and a comprehensive membrane mechanics model is needed. The theory of elastic membranes (Green & Adkins 1960) was developed for the in-plane stress, transverse shear tension and bending moment inside a membrane. Its coupling with an external flow field was utilized by Barthès-Biesel's group (Barthès-Biesel 1980; Barthès-Biesel & Rallison 1981; Barthès-Biesel & Sgaier 1985; Li, Barthès-Biesel & Helmy 1988; Leyrat-Maurin & Barthes-Biesel 1994; Quéguiner & Barthès-Biesel 1997; Diaz, Pelekasis & Barthès-Biesel 2000; Lac *et al.* 2004) and Pozrikidis's group (Pozrikidis 2001, 2003*a*,*b*, 2005) to simulate the flow-induced deformation of a capsule. In the present work, we will also incorporate the theory of elastic membranes into our theoretical analysis, based on an asymptotic expansion. Another difficulty in carrying out theoretical analysis on surface stability of an encapsulated bubble stems from the no-slip condition at the membrane. For a gas bubble, the kinematic condition in the normal direction determines the position of material points at the interface. For an encapsulated bubble, on the other hand, the material points move along the interface since the membrane bears in-plane stresses. For this reason, we must consider the motion in the tangential direction. Furthermore, the viscous effect is significant for a small bubble of micrometre size (Chapman & Plesset 1971). And due to the no-slip condition, the vorticity induced by deformation will influence the dynamics of the bubble and thus cannot be neglected. Tsiglifis & Pelekasis (2011) presented an analysis of the parametric stability of an encapsulated bubble based on potential flow theory, in which a free-slip condition on the bubble surface was employed. This irrotational model would be valid when the hydrodynamics is dominated by the kinematic condition associated with the interfacial displacement normal to the bubble surface rather than by the dynamic condition. However, for an encapsulated bubble, potential flow theory is insufficient when one studies the influence of the membrane dynamics on the hydrodynamics, since the dynamic condition must play a significant role. The membrane effect is reflected by the generation of the in-plane stress due to the interfacial displacement tangential to the bubble surface, which accounts for the frictional traction jump between the liquid and gas phases. Therefore, instead of potential flow theory, which is inadequate for describing the frictional traction jump, we employ the theory by Prosperetti (1977) that includes a viscous correction to Plesset's potential model. It should be noted that the theoretical approach by Prosperetti (1977) consisting of the boundary layer effect has been successfully applied to many complicated problems involving a change in bubble volume, for example, two-bubble interactions (Takahira, Akamatsu & Fujikawa 1991), sonoluminescing bubbles (Hilgenfeldt, Lohse & Brenner 1996), and shape instability in an acoustic field (Hao & Prosperetti 1999).

In this paper, we follow Prosperetti's method, and incorporate the theory of elastic membranes into the normal and tangential hydrodynamic balance. We use the derived system to map out the stability diagram as a function of driving pressure frequency versus amplitude. The present system involves the coupling of the nonlinear radial motion and the linear shape motion in the normal and tangential directions. Since the toroidal component of vorticity is included as in Prosperetti's model (1977), the system of governing equations has an integro-differential structure. To make clear the resonance interaction between the radial mode and the shape mode, we reduce the system to the form of Mathieu's equation by using a boundary layer approximation.

The expression for the natural frequency of the shape mode is thereby derived, as an extension with membrane effect from the formula (1.2).

The paper is organized as follows. In § 2, we formulate the problem and pay special attention to the boundary conditions at the bubble surface in §§ 2.2 and 2.3. The membrane mechanics is incorporated into the dynamic force balance, and the no-slip condition requires an additional velocity condition in the tangential direction. The derived system is reduced to Mathieu's equation by a boundary layer approximation in § 3. At the same time, the expression for the natural frequency of the shape mode is derived. In § 4, the stability diagram of driving amplitude versus driving frequency and the effects of viscosity are presented, respectively. The summary and conclusions are given in § 5.

2. Problem formulation

2.1. *General formulation*

We consider a single bubble suspended in an unbounded acoustic field. The driving pressure applied from the far field is characterized by a dimensionless amplitude ε and a driving frequency ω_d:

$$p_\infty = p_0(1 + \varepsilon \sin \omega_d t), \tag{2.1}$$

where p_0 is the ambient pressure. Owing to the negligible density and viscosity of gas inside the bubble relative to those of the external liquid, we do not solve the internal flow field directly. The liquid outside the bubble is water with density ρ and viscosity μ_l, which are assumed to be constant. The governing equations for the external flow field are the continuity equation and the incompressible Navier–Stokes equation, in the absence of body forces:

$$\nabla \cdot \boldsymbol{u} = 0, \tag{2.2}$$

$$\rho \frac{\partial \boldsymbol{u}}{\partial t} + \rho(\boldsymbol{u} \cdot \nabla)\boldsymbol{u} = -\nabla p + \mu_l \nabla \cdot (\nabla \boldsymbol{u} + \nabla \boldsymbol{u}^{\mathrm{T}}), \tag{2.3}$$

where $\boldsymbol{u}$ denotes the velocity vector, and p the liquid pressure. Unlike the gas bubble, the bubble encapsulated by a membrane bears a no-slip condition at the surface. In other words, the velocities at the membrane and at the attaching liquid side are equal not only in the normal direction but also in the tangential direction. The dynamic equilibrium at the bubble surface is described by a traction jump across the membrane. In addition, we provide a regularity condition at infinity. The above-mentioned boundary conditions are

$$\boldsymbol{u}_m = \boldsymbol{u}_l \quad \text{at } S = 0, \tag{2.4}$$

$$\boldsymbol{n} \cdot (-p\boldsymbol{I} + 2\mu_l \boldsymbol{E}) = \boldsymbol{n} \cdot (-p_g \boldsymbol{I}) + (\gamma \nabla \cdot \boldsymbol{n})\boldsymbol{n} + \boldsymbol{F} \quad \text{at } S = 0, \tag{2.5}$$

$$p \to p_\infty, \quad \boldsymbol{u} \to 0 \quad \text{as } r \to \infty, \tag{2.6}$$

where the subscripts m and l represent the material points at the membrane and the liquid side, respectively, S the surface function defined later in (2.36), $\boldsymbol{n}$ the unit normal vector pointing towards the liquid, $\boldsymbol{I}$ the unit tensor, $\boldsymbol{E}(= (\nabla \boldsymbol{u} + \nabla \boldsymbol{u}^{\mathrm{T}})/2)$ the strain rate tensor, p_g the gas pressure, γ the surface tension, and $\boldsymbol{F}$ the traction jump between the liquid and gas phases due to the presence of the membrane. The gas within the bubble is assumed to be uniformly distributed. In the present study, the gas pressure p_g is assumed to vary according to the polytropic process:

$$p_g = p_{g0} \left(V_0/V\right)^{\Gamma}, \tag{2.7}$$

where V denotes the bubble volume, and the subscript 0 indicates the initial value. $\varGamma$ is the effective polytropic index which includes thermal dissipation, defined by (Prosperetti 1991)

$$\varGamma = \tfrac{1}{3} Re \widetilde{F}. \tag{2.8}$$

The function $\widetilde{F}$ is

$$\widetilde{F} = \frac{3\zeta\eta^2}{\eta[\eta + 3(\zeta - 1)A_-] - 3i(\zeta - 1)(\eta A_+ - 2)}, \tag{2.9a}$$

$$\eta = R_0\sqrt{\frac{2\omega_0}{\psi}}, \quad A_\pm = \frac{\sinh\eta \pm \sin\eta}{\cosh\eta - \cos\eta}, \tag{2.9b}$$

where ζ is the ratio of specific heats, R_0 the initial radius, ω_0 the zeroth-order natural frequency, and ψ the thermal diffusivity. The calculated effective polytropic index is between 1.0 and 1.2 in the present work, which is reasonably close to the value of 1.1 chosen in Khismatullin (2004) and 1.07 in Tsiglifis & Pelekasis (2011). The viscosity of the gas is neglected. The surface tension γ is greatly reduced when the bubble is encapsulated by a membrane. We will retain the surface tension term here in order to keep the analysis complete. The membrane stress $\boldsymbol{F}$ is given by the surface divergence of the elastic tension tensor:

$$\boldsymbol{F} = -(\mathbf{P}\cdot\nabla)\cdot(\boldsymbol{\tau} + \boldsymbol{qn}), \tag{2.10}$$

where $\mathbf{P}(= \mathbf{I} - \boldsymbol{nn})$ is the tangential projection operator, $\boldsymbol{\tau}$ the in-plain stress and $\boldsymbol{q}$ the transverse shear tension.

We consider a viscoelastic membrane, which exhibits both viscous and elastic characteristics. The constitutive law of the elastic part is described by a Helmholtz free energy function (or strain energy function) W, and connects the in-plane stress with the surface strain thereon (Holzapfel 2000), while the viscous part is a linear resistance to the strain rate. In the directions of the principal stretches λ_i $(i = 1, 2)$, the respective principal components of the in-plane stress $\boldsymbol{\tau}$ are written as

$$\tau_i = \frac{\lambda_i}{\lambda_1\lambda_2}\frac{\partial W(\lambda_1, \lambda_2)}{\partial\lambda_i} + 2\mu_s\lambda_i\frac{\partial\lambda_i}{\partial t}, \quad i = 1, 2, \tag{2.11}$$

where μ_s is the surface membrane viscosity. We adopt the neo-Hookean law, a simple form of the strain-softening Mooney–Rivlin law (Mooney 1940), of which the strain energy function is given by

$$W = \frac{G_s}{2}\left(\lambda_1^2 + \lambda_2^2 + \frac{1}{\lambda_1^2\lambda_2^2} - 3\right), \tag{2.12}$$

where G_s denotes the surface modulus of elasticity. Although the neo-Hookean law cannot reveal the experimentally observed behaviour of a contrast agent, it allows us to perform modal analysis with respect to each deformation mode owing to its linearity, and the results therefrom should afford insight into the stability.

The transverse shear tension $\boldsymbol{q}$ is treated in terms of the bending moment $\boldsymbol{m}$:

$$\boldsymbol{q} = [(\mathbf{P}\cdot\nabla)\cdot\boldsymbol{m}]\cdot\mathbf{P}. \tag{2.13}$$

The bending moment is expressed by a bending strain energy function W_b in a similar form to that of the in-plain stress:

$$m_i = \frac{\lambda_i}{\lambda_1\lambda_2}\frac{\partial W_b(K_1, K_2)}{\partial K_i}, \quad i = 1, 2, \tag{2.14}$$

where K_i $(i = 1, 2)$ is the principal bending strain. We here write W_b in the form (Love 1888)

$$W_b = \frac{G_b}{2}(K_1^2 + 2\upsilon K_1 K_2 + K_2^2), \tag{2.15}$$

where G_b denotes the bending modulus and υ the Poisson ratio.

We consider nonlinearity induced by the spherical motion of a bubble subjected to a driving pressure, which yields the Rayleigh–Plesset equation, and then obtain the base flow. The deviated motion therefrom is regarded as a linear perturbation, and its temporal evolution is numerically computed to investigate the stability of the system.

To investigate the viscous effects, we follow Prosperetti's work (Prosperetti 1977) by dividing the velocity and pressure fields into three parts, respectively:

$$\boldsymbol{u} = \boldsymbol{u}_0 + \delta\boldsymbol{u}_p + \delta\boldsymbol{u}_v, \tag{2.16}$$

$$p = p_0 + \delta p_p + \delta p_v, \tag{2.17}$$

where the subscripts 0, p and v stand for the radial motion, the non-spherical correction, and the viscous correction to the potential flow, respectively. We shall restrict our attention to an axisymmetric system, so that we do not consider the azimuthal mode in the fluid flow or the interfacial deflection. It should be noted that due to the mobility of the membrane in both the radial and tangential directions, we introduce the deformation disturbance $\delta\Theta$ in the tangential direction as well as δf in the radial direction to describe the surface position (r_s, θ_s) as

$$r_s(\theta, t) = R(t) + \delta f(\theta, t), \tag{2.18}$$

$$\theta_s(\theta, t) = \theta + \delta\Theta(\theta, t)/R(t). \tag{2.19}$$

The disturbance functions f and Θ are expanded using the amplitudes of $a_k(t)$ and $b_k(t)$, respectively, in a series of (associated) Legendre polynomials $P_k(\cos\theta)$ and $P_k^1(\cos\theta)(= \mathrm{d}P_k(\cos\theta)/\mathrm{d}\theta)$:

$$f(\theta, t) = a_k(t)P_k(\cos\theta), \quad k \geqslant 2. \tag{2.20}$$

$$\Theta(\theta, t) = b_k(t)P_k^1(\cos\theta), \quad k \geqslant 2. \tag{2.21}$$

The general solutions of the velocity and pressure components in (2.16) and (2.17) can be found in Plesset (1954) and Prosperetti (1977) (see also Appendix A). The velocity vectors and the pressures on the bubble surface are

$$\boldsymbol{u}_0 = \frac{\dot{R}R^2}{r^2}\boldsymbol{e}_r, \tag{2.22}$$

$$\boldsymbol{u}_p = \frac{\left(\dot{a}_k + \dfrac{2\dot{R}a_k}{R}\right)R^{k+2}}{(k+1)r^{k+2}}\left[(k+1)P_k(\cos\theta)\boldsymbol{e}_r - P_k^1(\cos\theta)\boldsymbol{e}_\theta\right], \tag{2.23}$$

$$\boldsymbol{u}_v = \left(T(r, t)P_k(\cos\theta) - \frac{\partial\Phi}{\partial r}\right)\boldsymbol{e}_r - \frac{1}{r}\frac{\partial\Phi}{\partial\theta}\boldsymbol{e}_\theta, \tag{2.24}$$

$$p_0 = p_\infty + \rho\left(R\ddot{R} + \frac{3}{2}\dot{R}^2\right) - \delta\rho a_k \ddot{R} P_k(\cos\theta), \tag{2.25}$$

$$p_p = \frac{\rho P_k(\cos\theta)}{(k+1)}(R\ddot{a}_k + 3\dot{R}\dot{a}_k + 2\ddot{R}a_k), \tag{2.26}$$

$$p_v = k\left\{\mu_l T(R, t)/R + \rho(\dot{R}/R)\int_R^\infty [(R/s)^3 - 1]\,(R/s)^k\, T(s, t)\,\mathrm{d}s\right\} P_k(\cos\theta), \tag{2.27}$$

where

$$\begin{aligned}\varPhi = P_k(\cos\theta)&\left[\left(\alpha(t) + \frac{k+1}{2k+1}\int_R^r s^{-k}T(s, t)\,\mathrm{d}s\right) r^k\right.\\ &\left.+\left(\frac{k}{k+1}R^{2k+1}\alpha(t) + \frac{k}{2k+1}\int_R^r s^{k+1}T(s, t)\,\mathrm{d}s\right) r^{-(k+1)}\right],\end{aligned} \tag{2.28}$$

$$\alpha(t) = -\frac{k+1}{2k+1}\int_R^\infty s^{-k}T(s, t)\,\mathrm{d}s, \tag{2.29}$$

and $T(r, t)$ is the toroidal field (Prosperetti 1977), which yields

$$\rho\frac{\partial T}{\partial t} + \rho\frac{\partial}{\partial r}[\dot{R}\,(R/r)^2\, T] - \mu_l\frac{\partial^2 T}{\partial r^2} + \mu_l k(k+1)r^{-2}T = 0, \tag{2.30}$$

with the boundary condition $T \to 0$ as $r \to \infty$. T on the bubble surface is determined by satisfying the tangential force balance, as shown in § 2.2. For the governing equations, boundary conditions, and brief explanations of their derivations, see Appendix A.

2.2. *Dynamic balances at the encapsulating membrane*

2.2.1. *Liquid stresses on the deformed surface*

The dynamic balance equation (2.5), written in the normal and tangential directions, are

$$-p + 2\mu_l \boldsymbol{n}\boldsymbol{\cdot}\boldsymbol{E}\boldsymbol{\cdot}\boldsymbol{n} = -p_g + \gamma\nabla\boldsymbol{\cdot}\boldsymbol{n} + F_n, \tag{2.31}$$

$$2\mu_l \boldsymbol{n}\boldsymbol{\cdot}\boldsymbol{E}\boldsymbol{\cdot}\boldsymbol{t} = F_t. \tag{2.32}$$

Equation (2.31) is Laplace's law with an additional normal stress term F_n. Equation (2.32) is a dynamic balance for the frictional traction. The treatment of the membrane stresses in the normal direction F_n and the tangential direction F_t will be discussed in detail below. Several components of the strain rate tensor, which will be used in the later sections, are presented here in advance:

$$\begin{aligned}e_{rr} &= \frac{\partial u_r}{\partial r}\\ &= -\frac{2\dot{R}}{R} - \delta P_k(\cos\theta)\left[(k+2)\frac{\dot{a}_k}{R} + (2k-2)\frac{a_k\dot{R}}{R^2} + k(2k+1)R^{k-2}\alpha(t)\right],\end{aligned} \tag{2.33}$$

$$\begin{aligned}e_{r\theta} &= \frac{r}{2}\frac{\partial}{\partial r}\left(\frac{u_\theta}{r}\right) + \frac{1}{2r}\frac{\partial u_r}{\partial \theta}\\ &= \frac{\delta}{2k+2}P_k^1(\cos\theta)\left[(2k+4)\frac{\dot{a}_k}{R} + (4k+8)\frac{a_k\dot{R}}{R^2}\right.\\ &\quad\left. +\ (4k+2)R^{k-2}\alpha(t) - (k+1)\frac{T}{R}\right],\end{aligned} \tag{2.34}$$

$$
\begin{aligned}
e_{\theta\theta} &= \frac{1}{r}\frac{\partial u_\theta}{\partial \theta} + \frac{u_r}{r} \\
&= \frac{\dot{R}}{R} + \frac{\delta}{k+1}\left[\left(P_k(\cos\theta) + kP_k(\cos\theta) - \frac{d^2P_k(\cos\theta)}{d\theta^2}\right)\frac{\dot{a}_k}{R}\right. \\
&\quad - \left[(k+1)P_k(\cos\theta) + 2\frac{d^2P_k(\cos\theta)}{d\theta^2}\right]\frac{a_k\dot{R}}{R^2} \\
&\quad \left. - \ (2k+1)\frac{d^2P_k(\cos\theta)}{d\theta^2}R^{k-2}\alpha(t)\right].
\end{aligned}
\tag{2.35}
$$

Next we introduce a surface function,

$$
S \equiv r_s - R(t) - \delta f(\theta, t) = 0, \tag{2.36}
$$

and denote the interface by $S = 0$. The unit normal vector $\boldsymbol{n}$ and the tangential one $\boldsymbol{t}$ are thereby written as

$$
\boldsymbol{n} = \frac{\boldsymbol{\nabla} S}{|\boldsymbol{\nabla} S|} \simeq \boldsymbol{e}_r - \delta\frac{1}{r}\frac{\partial f}{\partial \theta}\boldsymbol{e}_\theta, \tag{2.37}
$$

$$
\boldsymbol{t} \simeq \boldsymbol{e}_\theta + \delta\frac{1}{r}\frac{\partial f}{\partial \theta}\boldsymbol{e}_r. \tag{2.38}
$$

Note that only f (or a_k) determines the bubble shape. Therefore, Θ should be linked not to the kinematic condition but to the continuity of the velocity as detailed in § 2.3. The curvature κ involved in (2.31), accounting for the Laplace pressure, is

$$
\begin{aligned}
\boldsymbol{\nabla}\boldsymbol{\cdot}\boldsymbol{n} &= \frac{2}{R} - \delta\left[2f + \frac{\cos\theta}{\sin\theta}\frac{\partial f}{\partial\theta} + \frac{\partial^2 f}{\partial\theta^2}\right]\frac{1}{R^2} \\
&= \frac{2}{R} + \delta(k+2)(k-1)\frac{f}{R^2}.
\end{aligned}
\tag{2.39}
$$

In consideration of (2.33)–(2.39), the force balance equations (2.31) and (2.32) are explicitly written as

$$
\begin{aligned}
&-(p_0 + \delta p_p + \delta p_v) + p_g + 2\mu_l\left(e_{rr} - \delta e_{r\theta}\frac{2a_k}{r}P_k^1(\cos\theta)\right) \\
&\quad -\gamma\left[\frac{2}{R} + \delta(k+2)(k-1)\frac{a_kP_k(\cos\theta)}{R^2}\right] = F_n,
\end{aligned}
\tag{2.40}
$$

and

$$
2\mu_l\left[e_{r\theta} - \delta e_{\theta\theta}\frac{a_k}{r}P_k^1(\cos\theta) + \delta e_{rr}\frac{a_k}{r}P_k^1(\cos\theta)\right] = F_t. \tag{2.41}
$$

The membrane stresses F_n and F_t are expanded up to $O(\delta)$ into, respectively,

$$
F_n = F_n^0 + \delta F_n^1, \tag{2.42}
$$

$$
F_t = \delta F_t^1. \tag{2.43}
$$

In the subsequent development, the components F_n^0, F_n^1 and F_t^1 are determined in consideration of the membrane constitutive law introduced in § 2.1.

2.2.2. *Surface deformation*

In spherical coordinates, one of the principal directions is the meridional direction (θ-direction); the other is the azimuthal direction (ϕ-direction) (see figure 1).

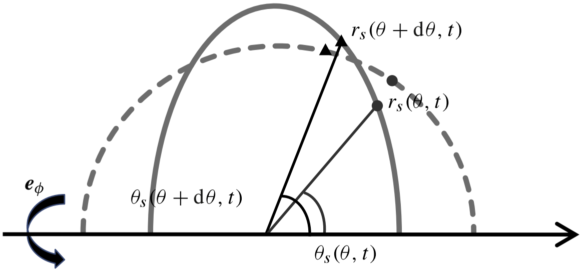

FIGURE 1. Sketch of bubble geometry.

Following the derivation by Tsiglifis & Pelekasis (2011), the two principal stretches are calculated by the extension ratio in the arclength direction and the change ratio of the distance from the axis of symmetry, i.e.

$$\lambda_1 = \lambda_\theta = \frac{\mathrm{d}s}{\mathrm{d}s^R} = \frac{R}{R_0} + \delta \frac{f}{R_0} + \delta \frac{1}{R_0}\frac{\partial \Theta}{\partial \theta}, \tag{2.44}$$

$$\lambda_2 = \lambda_\phi = \frac{r \sin\theta}{(r\sin\theta)^R} = \frac{R}{R_0} + \delta \frac{f}{R_0} + \delta \frac{\Theta}{R_0}\cot\theta, \tag{2.45}$$

where the superscript R represents the reference configuration. In the following, we assume that the initial state is unstressed, so that it corresponds to the reference state.

2.2.3. *In-plane stress*

The in-plane stress $\boldsymbol{\tau}$ up to $O(\delta^1)$ is expressed in the form of principal components in spherical coordinates:

$$\boldsymbol{\tau} = \tau_\theta \boldsymbol{e}_\theta \boldsymbol{e}_\theta + \tau_\phi \boldsymbol{e}_\phi \boldsymbol{e}_\phi. \tag{2.46}$$

Here, τ_θ and τ_ϕ are derived from the surface energy function according to (2.11) and (2.12):

$$\begin{aligned}
\tau_\theta &= \frac{G_s}{\lambda_\theta \lambda_\phi}\left(\lambda_\theta^2 - \frac{1}{\lambda_\theta^2 \lambda_\phi^2}\right) + 2\mu_s \frac{1}{\lambda_\theta}\frac{\partial \lambda_\theta}{\partial t} \\
&= G_s\left(1 - \frac{R_0^6}{R^6}\right) + 2\mu_s \frac{\dot{R}}{R} \\
&\quad + \delta G_s\left(\frac{6f R_0^6}{R^7} - \frac{\Theta \cot\theta}{R} + \frac{3\Theta R_0^6 \cot\theta}{R^7} + \frac{1}{R}\frac{\partial \Theta}{\partial \theta} + \frac{3R_0^6}{R^7}\frac{\partial \Theta}{\partial \theta}\right) \\
&\quad + 2\delta\mu_s\left(-\frac{f\dot{R}}{R^2} + \frac{1}{R}\frac{\partial f}{\partial t} - \frac{\dot{R}}{R^2}\frac{\partial \Theta}{\partial \theta} + \frac{1}{R}\frac{\partial^2 \Theta}{\partial \theta \partial t}\right),
\end{aligned} \tag{2.47}$$

and

$$\begin{aligned}
\tau_\phi &= \frac{G_s}{\lambda_\theta \lambda_\phi}\left(\lambda_\phi^2 - \frac{1}{\lambda_\theta^2 \lambda_\phi^2}\right) + 2\mu_s \frac{1}{\lambda_\phi}\frac{\partial \lambda_\phi}{\partial t} \\
&= G_s\left(1 - \frac{R_0^6}{R^6}\right) + 2\mu_s \frac{\dot{R}}{R} \\
&\quad + \delta G_s\left(\frac{6f R_0^6}{R^7} + \frac{\Theta \cot\theta}{R} + \frac{3\Theta R_0^6 \cot\theta}{R^7} - \frac{1}{R}\frac{\partial \Theta}{\partial \theta} + \frac{3R_0^6}{R^7}\frac{\partial \Theta}{\partial \theta}\right) \\
&\quad + 2\delta\mu_s\left(-\frac{f\dot{R}}{R^2} + \frac{1}{R}\frac{\partial f}{\partial t} - \frac{\dot{R}\Theta \cot\theta}{R^2} + \frac{\cot\theta}{R}\frac{\partial \Theta}{\partial t}\right).
\end{aligned} \tag{2.48}$$

2.2.4. *Bending moment*

Before deriving the transverse shear tension $\boldsymbol{q}$, we first consider the curvatures along the principal directions. The principal curvature comes from the curvature tensor $\boldsymbol{B}$, defined as

$$\boldsymbol{B} = \boldsymbol{P} \cdot \nabla \boldsymbol{n}, \tag{2.49}$$

where $\boldsymbol{P}$ is the tangential projection operator, written as

$$\boldsymbol{P} = \boldsymbol{I} - \boldsymbol{n}\boldsymbol{n} = \boldsymbol{e}_\theta \boldsymbol{e}_\theta + \boldsymbol{e}_\phi \boldsymbol{e}_\phi + \delta \frac{1}{r}\frac{\partial f}{\partial \theta} \boldsymbol{e}_\theta \boldsymbol{e}_r + \delta \frac{1}{r}\frac{\partial f}{\partial \theta} \boldsymbol{e}_r \boldsymbol{e}_\theta. \tag{2.50}$$

Substituting the expression of the unit normal vector $\boldsymbol{n}$ (2.37) into (2.49), we obtain the curvature tensor,

$$\boldsymbol{B} = \left[\frac{1}{R} - \delta\left(\frac{f}{R^2} + \frac{1}{R^2}\frac{\partial^2 f}{\partial \theta^2}\right)\right] \boldsymbol{e}_\theta \boldsymbol{e}_\theta + \left[\frac{1}{R} - \delta\left(\frac{f}{R^2} + \frac{\cot\theta}{R^2}\frac{\partial f}{\partial \theta}\right)\right] \boldsymbol{e}_\phi \boldsymbol{e}_\phi, \tag{2.51}$$

from which we obtain two principal curvatures in the θ- and ϕ-directions:

$$\kappa_\theta = \frac{1}{R} - \delta\left(\frac{f}{R^2} + \frac{1}{R^2}\frac{\partial^2 f}{\partial \theta^2}\right), \tag{2.52}$$

and

$$\kappa_\phi = \frac{1}{R} - \delta\left(\frac{f}{R^2} + \frac{\cot\theta}{R^2}\frac{\partial f}{\partial \theta}\right). \tag{2.53}$$

The summation of these two principal curvatures is consistent with (2.39), another way to calculate the average curvature. We define two bending strains K_θ and K_ϕ under the assumption of small deformation:

$$K_\theta = \lambda_\theta \kappa_\theta - \kappa_\theta^R, \quad K_\phi = \lambda_\phi \kappa_\phi - \kappa_\phi^R. \tag{2.54}$$

Note that (2.54) is formulated to guarantee no bending strain in a purely radial oscillation. The bending moment $\boldsymbol{m}$ is decomposed into two principal components:

$$\boldsymbol{m} = m_\theta \boldsymbol{e}_\theta \boldsymbol{e}_\theta + m_\phi \boldsymbol{e}_\phi \boldsymbol{e}_\phi. \tag{2.55}$$

The components are calculated by the bending energy function ((2.14) and (2.15)). We obtain

$$\begin{aligned} m_\theta &= \frac{G_b}{\lambda_\phi}(K_\theta + \upsilon K_\phi) \\ &= \delta \frac{G_b}{R^2}\left[\frac{\partial \Theta}{\partial \theta} - \frac{\partial^2 f}{\partial \theta^2} + \upsilon \cot\theta \left(\Theta - \frac{\partial f}{\partial \theta}\right)\right], \end{aligned} \tag{2.56}$$

and

$$\begin{aligned} m_\phi &= \frac{G_b}{\lambda_\theta}(K_\phi + \upsilon K_\theta) \\ &= \delta \frac{G_b}{R^2}\left[\cot\theta \left(\Theta - \frac{\partial f}{\partial \theta}\right) + \upsilon \left(\frac{\partial \Theta}{\partial \theta} - \frac{\partial^2 f}{\partial \theta^2}\right)\right]. \end{aligned} \tag{2.57}$$

Since the bending moments are of the order $O(\delta^1)$, (2.13) immediately implies $\boldsymbol{q} \sim O(\delta^1)$. Equation (2.13) is rewritten as

$$\boldsymbol{q} = \left[\frac{1}{r}\frac{\partial m_\theta}{\partial \theta} + \frac{\cos\theta}{r \sin\theta}(m_\theta - m_\phi)\right] \boldsymbol{e}_\theta \equiv q \boldsymbol{e}_\theta. \tag{2.58}$$

2.2.5. *Force balance up to $O(\delta^1)$*

Substituting the component form of in-plane stress (2.46) and transverse shear tension (2.58) into (2.10), we obtain the expression for membrane stress:

$$\begin{aligned}\boldsymbol{F} &= \left[\frac{1}{r}(\tau_\theta + \tau_\phi) - \frac{q\cos\theta}{r\sin\theta} - \frac{1}{r}\frac{\partial q}{\partial\theta}\right]\boldsymbol{e}_r \\ &\quad + \left[\frac{\cos\theta}{r\sin\theta}(\tau_\phi - \tau_\theta) - \frac{q}{r} - \frac{1}{r}\frac{\partial\tau_\theta}{\partial\theta} + \delta\left(\frac{\tau_\theta}{r^2}\frac{\partial f}{\partial\theta}\right)\right]\boldsymbol{e}_\theta \\ &\equiv F_n\boldsymbol{e}_r + F_t\boldsymbol{e}_\theta.\end{aligned} \tag{2.59}$$

Considering the specific forms of a neo-Hookean material (2.47) and (2.48), the components in (2.42) and (2.43) are obtained as follows:

$$F_n^0 = \frac{2G_s(R^6 - R_0^6)}{R^7} + 4\mu_s\frac{\dot{R}}{R^2}, \tag{2.60}$$

$$\begin{aligned}F_n^1 &= -\frac{G_s}{R^8}[2(R^6 - 7R_0^6)a_k + 6k(k+1)R_0^6 b_k]P_k(\cos\theta) \\ &\quad + \frac{G_b}{R^4}[k(k+1)(k^2 + k - 1 + \upsilon)(a_k - b_k)]P_k(\cos\theta) \\ &\quad + \frac{2\mu_s}{R^3}[-4a_k\dot{R} + 2R\dot{a}_k + k(k+1)(\dot{R}b_k - R\dot{b}_k)]P_k(\cos\theta),\end{aligned} \tag{2.61}$$

$$\begin{aligned}F_t^1 &= \frac{G_s}{R^8}\{(R^6 - 7R_0^6)a_k + [3k(k+1)R_0^6 + (k-1)(k+2)R^6]b_k\}P_k^1(\cos\theta) \\ &\quad - \frac{G_b}{R^4}(k^2 + k - 1 + \upsilon)(a_k - b_k)P_k^1(\cos\theta) \\ &\quad + \frac{2\mu_s}{R^3}[2\dot{R}a_k - R\dot{a}_k + (k^2 + k - 1)(R\dot{b}_k - \dot{R}b_k)]P_k^1(\cos\theta).\end{aligned} \tag{2.62}$$

Substituting the membrane stresses (2.60)–(2.62) into the normal and tangential force balance (2.40) and (2.41) together with the expressions of velocity vectors and pressures (2.22)–(2.29) and the components of the strain rate tensor (2.33)–(2.35), we obtain the final expressions of force balance:

$$R\ddot{R} + \frac{3}{2}\dot{R}^2 + \frac{1}{\rho}\left[\frac{2\gamma}{R} + 4\mu_l\frac{\dot{R}}{R} - p_g + p_\infty + \frac{2G_s(R^6 - R_0^6)}{R^7} + 4\mu_s\frac{\dot{R}}{R^2}\right] = 0, \tag{2.63}$$

$$\begin{aligned}&\frac{\rho R}{k+1}\ddot{a}_k + \left[\frac{3\rho}{k+1}\dot{R} - \frac{2\mu_l(k+2)(k-1)}{R}\right]\dot{a}_k \\ &\quad + \left[-\frac{k-1}{k+1}\rho\ddot{R} + 2\mu_l(k-1)(k+2)\frac{\dot{R}}{R^2} + (k-1)(k+2)\frac{\gamma}{R^2}\right]a_k \\ &\quad + \mu_l k(k+2)\frac{T(R,t)}{R} + k\rho\frac{\dot{R}}{R}\int_R^\infty [(R/s)^3 - 1]\,(R/s)^k\,T(s,t)\,\mathrm{d}s \\ &\quad + \frac{G_s(k-1)(k+2)}{R^8}[(R^6 - 7R_0^6)a_k + k(k+1)(3R_0^6 + R^6)b_k] \\ &\quad + \frac{2\mu_s(k-1)(k+2)}{R^3}[(2a_k\dot{R} - R\dot{a}_k) + k(k+1)(R\dot{b}_k - \dot{R}b_k)] = 0, \quad k \geqslant 2,\end{aligned} \tag{2.64}$$

$$\mu_l\left[(2k+4)\frac{\dot{a}_k}{R} - (2k-2)\frac{a_k\dot{R}}{R^2} - (k+1)\frac{T(R,t)}{R} + (4k+2)R^{k-2}\alpha(t)\right]$$

$$\begin{aligned} &= \frac{G_s(k+1)}{R^8}\{(R^6 - 7R_0^6)a_k + [3k(k+1)R_0^6 + (k-1)(k+2)R^6]b_k\} \\ &\quad + \frac{G_b}{R^4}(k+1)(k^2+k-1+\upsilon)(b_k - a_k) \\ &\quad + \frac{2\mu_s(k+1)}{R^3}[2\dot{R}a_k - R\dot{a}_k + (k^2+k-1)(R\dot{b}_k - \dot{R}b_k)]. \end{aligned} \tag{2.65}$$

Equation (2.63) describes the radial motion and determines the base flow. It has a similar form to the Rayleigh–Plesset equation. The additional terms $2G_s(R^6 - R_0^6)/(\rho R^7) + 4\mu_s\dot{R}/R^2$ account for the membrane stress and viscous damping, which are applicable to large deformation membrane dynamics. Linearizing this equation under the assumption of $|R/R_0 - 1| \ll 1$, we obtain a harmonic oscillator equation, from which we find the zeroth-order natural frequency:

$$\omega_0 = \sqrt{3\Gamma\frac{p_{g0}}{\rho R_0^2} - \frac{2\gamma}{\rho R_0^3} + \frac{12G_s}{\rho R_0^3}}. \tag{2.66}$$

This expression in the limit of the infinitesimal radius change has the same form as that derived from an exponential model developed by Kviklienė *et al.* (2004). Equation (2.64) describes the dynamics of shape modes. The amplitudes in two directions a_k and b_k are coupled. However, only a_k determines the bubble's shape. Equation (2.65) is the tangential balance at the membrane. It will be used in obtaining the solution of the toroidal field as a boundary condition.

2.3. *Tangential velocity boundary condition*

The kinematic condition in the normal direction is the same as the treatment in the gas bubble case, and is used to derive the irrotational velocity field (see Appendix A). For a gas bubble, once the free-slip boundary condition is imposed on the surface, the tangential velocity is given. For the encapsulated bubble, on the other hand, not only the dynamic condition (2.65) but also the continuity of the tangential velocity component must be considered. Since the liquid motion on the surface is assumed to be attached to the membrane, we employ a no-velocity-jump condition

$$u_\theta = r_s\frac{\partial\theta_s}{\partial t}, \tag{2.67}$$

of which the left-hand side is given by (2.23) and (2.24), while the right-hand side is given by (2.18) and (2.19). Hence, using b_k, (2.67) is explicitly written as

$$\dot{b}_k - \frac{\dot{R}}{R}b_k = -\frac{\dot{a}_k + \dfrac{2\dot{R}a_k}{R}}{k+1} + R^{k-1}\int_R^\infty s^{-k}T(s,t)\,\mathrm{d}s. \tag{2.68}$$

3. Structure of Mathieu's equation

Equations (2.64) and (2.68) are integro-differential equations, in which the integrals are related to the toroidal field. Moreover, the amplitudes a_k and b_k are coupled. At first glance, it appears difficult to obtain an analytic expression for the higher-order natural frequency such as (1.2) for the gas bubble. However, we notice that the vorticity produced by the deformation of the membrane is usually restricted to a thin boundary layer. The boundary layer approximation has been frequently used in previous analyses of Prosperetti's model (Brenner, Lohse & Dupont 1995; Hilgenfeldt *et al.* 1996; Hao & Prosperetti 1999; An, Lu & Yang 2005; Holzfuss 2008). The thickness of the boundary layer is defined as (Hilgenfeldt *et al.* 1996)

$$\chi = \min\left(\sqrt{\frac{\mu_l}{\rho\omega_0}}, \frac{R}{2k}\right). \tag{3.1}$$

In this way, the integrals in (2.64), (2.65) and (2.68) are approximated by the integrand being evaluated at the bubble surface multiplied by the thickness of the boundary layer, i.e.

$$\int_R^\infty [(R/s)^3 - 1]\,(R/s)^k\, T(s, t)\,\mathrm{d}s \approx 0, \tag{3.2}$$

and

$$\int_R^\infty s^{-k} T(s, t)\,\mathrm{d}s \approx R^{-k} T(R, t)\,\chi. \tag{3.3}$$

Replacing the integrals in (2.64) and (2.65) and eliminating $T(R, t)$ using the tangential velocity boundary condition (2.68), we obtain the following set of equations,

$$\ddot{a}_k + C_{a1}\dot{a}_k + C_{b1}\dot{b}_k + C_a a_k + C_b b_k = 0, \tag{3.4}$$

$$D_{b1}\dot{b}_k + D_b b_k + D_{a1}\dot{a}_k + D_a a_k = 0, \tag{3.5}$$

where the coefficients are

$$\begin{aligned} C_{a1} = {} & \frac{3\dot{R}}{R} + \left[-2(k+2)(k^2-1) + \frac{k(k+2)R}{\chi}\right]\frac{\mu_l}{\rho R^2} \\ & - (k-1)(k+1)(k+2)\frac{2\mu_s}{\rho R^3}, \end{aligned} \tag{3.6}$$

$$C_{b1} = k(k+1)(k+2)\frac{\mu_l}{\rho\chi R} + k(k-1)\,(k+1)^2(k+2)\frac{2\mu_s}{\rho R^3}, \tag{3.7}$$

$$\begin{aligned} C_a = {} & -(k-1)\frac{\ddot{R}}{R} + \left[(k-1)(k+1)(k+2) + \frac{k(k+2)R}{\chi}\right]\frac{2\mu_l\dot{R}}{\rho R^3} \\ & + (k-1)(k+1)(k+2)\frac{4\mu_s\dot{R}}{\rho R^4} + (k-1)(k+1)(k+2)\frac{\gamma}{\rho R^3} \\ & + (k-1)(k+1)(k+2)(R^6 - 7R_0^6)\frac{G_s}{\rho R^9}, \end{aligned} \tag{3.8}$$

$$\begin{aligned} C_b = {} & k(k-1)\,(k+1)^2(k+2)(R^6 + 3R_0^6)\frac{G_s}{\rho R^9} \\ & - k(k+1)(k+2)\frac{\mu_l\dot{R}}{\rho\chi R^2} - 2k(k-1)\,(k+1)^2(k+2)\frac{\mu_s\dot{R}}{\rho R^4}, \end{aligned} \tag{3.9}$$

$$D_{b1} = -(k+1)\left(\frac{2}{R} + \frac{1}{\chi}\right)\mu_l - (k+1)(k^2+k-1)\frac{2\mu_s}{R^2}, \tag{3.10}$$

$$\begin{aligned} D_b = {} & (k+1)\left(2 + \frac{R}{\chi}\right)\frac{\mu_l\dot{R}}{R^2} + (k+1)(k^2+k-1)\frac{2\mu_s\dot{R}}{R^3} \\ & - (k+1)[(k-1)(k+2)R^6 + 3k(k+1)R_0^6]\frac{G_s}{R^8} \\ & - (k+1)(k^2+k-1+\upsilon)\frac{G_b}{R^4}, \end{aligned} \tag{3.11}$$

$$D_{a1} = \mu_l\left[-\frac{1}{\chi} + \frac{2(k+1)}{R}\right] + 2\mu_s\frac{k+1}{R^2}, \tag{3.12}$$

$$
\begin{aligned}
D_a = & -\left(k+1+\frac{R}{\chi}\right)\frac{2\mu_l\dot{R}}{R^2} - (k+1)\frac{4\mu_s\dot{R}}{R^3} \\
& - (k+1)(R^6 - 7R_0^6)\frac{G_s}{R^8} + (k+1)(k^2+k-1+\upsilon)\frac{G_b}{R^4}.
\end{aligned}
\tag{3.13}
$$

Equation (3.4) is essentially the dynamic force balance in the normal direction, while (3.5) is that in the tangential direction.

Next, we analyse the order of magnitude for the terms in (3.6)–(3.13). Equations (3.10) and (3.12) are of the order of $((\mu_l/R) + (\mu_s/R^2))$, much smaller than that of $((G_s/R^2) + (G_b/R^4))$ in (3.11) and (3.13). Accordingly, (3.5) can be simplified as

$$
D_b b_k + D_a a_k = 0. \tag{3.14}
$$

For (3.6)–(3.9), similarly, we drop the terms of the order of $((\mu_l/\rho R^2) + (\mu_s/\rho R^3))$, which are much smaller than those of the order of $(G_s/(\rho R^3))$. Then we eliminate b_k in (3.4) by using (3.14) and rearranging the coefficient and obtain a differential equation for a_k:

$$
\ddot{a}_k + C'_{a1}\dot{a}_k + C'_a a_k = 0, \tag{3.15}
$$

where

$$
C'_{a1} = \frac{3\dot{R}}{R}, \tag{3.16}
$$

$$
\begin{aligned}
C'_a = & -(k-1)\frac{\ddot{R}}{R} + k(k+2)\frac{2\mu_l\dot{R}}{\rho\chi R^2} \\
& + (k-1)(k+1)(k+2)\left[\frac{\gamma}{\rho R^3} + \frac{2\mu_l\dot{R}}{\rho R^3} + \frac{4\mu_s\dot{R}}{\rho R^4} + \frac{(R^6-7R_0^6)G_s}{\rho R^9}\right] \\
& + \left\{k(k-1)(k+1)(k+2)\left[\frac{(R^6+3R_0^6)G_s}{\rho R^7} - \frac{2\mu_s\dot{R}}{\rho R^2}\right] - k(k+2)\frac{\mu_l\dot{R}}{\rho\chi}\right\} \\
& \times \left\{(k+1)\left[\frac{2\mu_l\dot{R}}{R^2} + \frac{4\mu_s\dot{R}}{R^3} + \frac{(R^6-7R_0^6)G_s}{R^8}\right.\right. \\
& \left.\left. - (k^2+k-1+\upsilon)\frac{G_b}{R^4}\right] + \frac{2\mu_l\dot{R}}{\chi R}\right\} \Big/ \left\{\left(2+\frac{R}{\chi}\right)\mu_l\dot{R} + (k^2+k-1)\frac{2\mu_s\dot{R}}{R}\right. \\
& \left. - \ [(k-1)(k+2)R^6 + 3k(k+1)R_0^6]\frac{G_s}{R^8} - (k^2+k-1+\upsilon)\frac{G_b}{R^4}\right\}.
\end{aligned}
\tag{3.17}
$$

Equation (3.15) is a standard linear oscillation equation, of which the coefficient before a_k represents the natural frequency. If the transient variation of R is neglected, the k-th order natural frequency is obtained as

$$
\begin{aligned}
\omega_k^2 = & (k-1)(k+1)(k+2)\frac{\gamma}{\rho R_0^3} + (k-1)(k+1)(k+2)\frac{2G_s}{\rho R_0^3} \\
& \times \frac{(2k^2+2k-3)(k^2+k-1+\upsilon)G_b + 6G_sR_0^2}{(k^2+k-1+\upsilon)G_b + 2(2k^2+2k-1)G_sR_0^2}.
\end{aligned}
\tag{3.18}
$$

This expression adds the effect of the membrane to the well-known formula for the higher-order natural frequency of a gas bubble (1.2). We compare the derived natural frequencies with those of our previous numerical simulation by means of a boundary-fitted finite volume method (Liu *et al.* 2011) and find good agreement (figure 2).

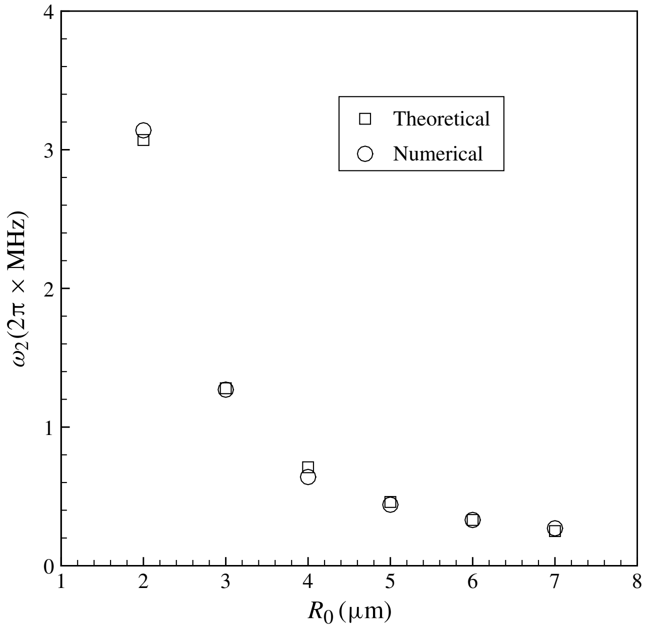

FIGURE 2. Natural frequencies compared with our previous numerical results by means of a boundary-fitted finite volume method.

It is well known that the dynamic equation of the shape mode for a gas bubble has the structure of Mathieu's equation, which characterizes the parametric resonance (Benjamin 1964). Following the procedure for a gas bubble, we introduce a transformation,

$$a_k = R^{-3/2}\alpha_k, \tag{3.19}$$

and assume that the bubble experiences a sinusoidal volume oscillation around the equilibrium radius driven by the imposed pressure wave:

$$R = R_0(1 + \epsilon \cos \omega_d t). \tag{3.20}$$

Substituting (3.19) and (3.20) into (3.15), we obtain

$$\ddot{\alpha}_k + G(t)\alpha_k = 0, \tag{3.21}$$

where

$$G(t) = \frac{\omega_k^2}{\omega_d^2} + \left[\frac{M}{\omega_d^2} + \left(k + \frac{1}{2}\right)\right] \epsilon \cos \tau, \tag{3.22}$$

where

$$\begin{aligned} M = &-(k-1)(k+1)(k+2)\frac{3\gamma}{\rho R_0^3} \\ &- \frac{2(k^3 + 2k^2 - k - 2)G_s}{\rho R_0^3\left[(k^2 + k - 1 + \upsilon)G_b + 2(2k^2 + 2k - 1)G_s R_0^2\right]^2} \\ &\times \Big[15(k^2 + k - 2)\,(k^2 + k - 1 + \upsilon)^2\, G_b^2 \end{aligned}$$

$$+ 8(5k^4 + 10k^3 - 11k^2 - 16k + 15)(k^2 + k - 1 + \upsilon) G_b G_s R_0^2$$
$$+ \; 6(22k^2 + 22k - 20) G_s^2 R_0^4 \big] \, . \tag{3.23}$$

Equation (3.21) has the structure of Mathieu's equation (Bender & Orszag 1978). The coefficient before α_k (3.22) is similar to that for a gas bubble, except for the parameter M (3.23) which includes the effects of the membrane. This difference, however, does not influence the stability condition of the equation, which is identical to that of a gas bubble:

$$\frac{\omega_k^2}{\omega_d^2} = \frac{n^2}{4}, \tag{3.24}$$

where n is an integer.

4. Results and discussion

In this section, we will solve the system formulated in § 2. At the initial state ($t = 0$), the flow field is assumed to be static, and an initial disturbance is set to $a_k = 0.1 R_0$. Giving the initial disturbance to b_k would not influence the results since a_k and b_k are coupled. The bubble radius R, and the shape mode variations a_k and b_k therefrom are computed numerically by solving the integro-differential equation set of (2.63), (2.64) and (2.68). For time integration, the fourth-order Runge–Kutta method is employed. The integrals are calculated by using composite numerical quadratures. The toroidal field $T(r, t)$ is temporally updated by solving the partial differential equation (2.30) using a finite difference method with the boundary conditions at the bubble surface (2.65) and $T \rightarrow 0$ at infinity. For details of the numerical treatment, see Appendix B.

4.1. *Stability diagram*

We apply an ultrasonic pressure with a non-dimensional amplitude $\varepsilon = 0.8$ and an ambient pressure $p_0 = 1 \times 10^5$ Pa. Since the parametric instability requires a finite time to develop, we impose 100 driving cycles. First we sweep in the radial direction, starting from 1 μm with increments of 0.2 μm, and set the driving frequency equal to the zeroth-order natural frequency, $\omega_d = \omega_0$, where ω_0 is calculated by (2.66). This is the condition of radial resonance, under which the radial oscillation tends to display a single frequency, which makes the investigation of the relationship between zeroth-order and higher-order natural frequencies straightforward. Five elastic moduli $G_s = 0.1, 0.3, 0.5, 0.7$ and 0.9 N m^{-1} are selected according to a practical range for a contrast agent (Hoff 2001; van der Meer *et al.* 2007). The surface membrane viscosity is taken to be the membrane viscosity multiplied by the membrane thickness, which equals to 10^{-8} kg s^{-1}, the same order as those in Hoff (2001) and van der Meer *et al.* (2007). There are few experimental measurements for the bending modulus G_b. In numerical simulations, the absence of bending resistance would lead to numerical instability, which physically results from buckling under compression (Pozrikidis 1990). Here we set $G_b = 2 \times 10^{-13}$ N m according to our previous numerical work (Liu *et al.* 2011), which is consistent with the value chosen by Pozrikidis (2001) and Tsiglifis & Pelekasis (2011).

The minimal radii for the onset of second-order shape instability are listed in table 1, along with the relevant zeroth- and second-order natural frequencies, which are calculated by (2.66) and (3.18). Here the condition of instability is defined

G_s (N m^{-1})	0.1	0.3	0.5	0.7	0.9
R_0 (μm)	5.8	8.6	10	10.4	10.6
ω_0 ($2\pi \times 10^6$ Hz)	0.64	0.51	0.49	0.52	0.55
ω_2 ($2\pi \times 10^6$ Hz)	0.35	0.29	0.29	0.32	0.36
ω_2/ω_0	0.56	0.57	0.60	0.63	0.65

TABLE 1. The threshold radius of instability and the relevant zeroth- and second-order resonance frequencies corresponding to the specific elastic modulus.

as $|a_k|/R_0 > 1$, that is, when the amplitude of the shape oscillation is greater than the initial radius. Since the stability analysis is restricted in the context of linearity, the initial disturbance to the shape mode will either decay to zero or grow exponentially, representing the stable or unstable situation. The data in table 1 reveal that the critical radius increases with the elastic modulus. In other words, the instability emerges in a bigger bubble for a larger value of the elastic modulus. In comparison to gas bubbles, for which the bigger ones are less stable, we can infer that the membrane stabilizes the shape oscillation. In addition, we can see from table 1 that the ratios between ω_2 and ω_0 are around 0.6, which agrees with the finding in Tsiglifis & Pelekasis (2011). Finally, our results are consistent with the stability condition of Mathieu's equation that the frequency of the radial oscillation approximates twice that of the second-order natural frequency, i.e. $\omega_d = \omega_0 \approx 2\omega_2$.

The evolutions of instability of the second-order shape mode as well as the radial oscillation for each case in table 1 are illustrated in figure 3. The radial mode (the dotted line) oscillates in a stable manner after the transient stage at the beginning, while the higher-order shape mode (the solid line) grows after tens of cycles of pressure driving. A closer inspection reveals that the second-order shape mode experiences a subharmonic oscillation, whose period approximates twice that of the zeroth-order mode. The integer ratio of the zeroth- and second-order natural frequencies sheds light on the subharmonic oscillation. In contrast, the bubbles with smaller radii which are below the critical value are stable; the initial disturbances to the shape mode decay quickly due to the influence of viscosity (see figure 4).

Figure 5 illustrates the phase diagram of shape stabilities of the five encapsulated bubbles in table 1, and that of the gas bubble. The phase diagram is plotted as a function of the driving frequency normalized by the second-order natural frequency ω_d/ω_2 and the thresholds of the driving pressure amplitude ε. The curves in figure 5 represent the borderlines of stability above which the shape oscillations become unstable, while below them the surface instabilities do not occur. Generally speaking, the oscillations behave in a more stable way above resonance than below resonance. For extremely high driving frequency, a strong driving pressure is needed to induce the shape modes. This is understandable because under high driving frequency, the oscillatory period is so short that the surface instability has insufficient time in which to develop. Most significantly, it is found that minima appear in the vicinity of $\omega_d/\omega_2 = 2$ for all of the encapsulated and gas bubbles, and secondary minima emerge in the neighbourhood of $\omega_d/\omega_2 = 1$. These unstable situations can be explained by the structure of Mathieu's equation in the system, which are the so-called one–two resonance and one–one resonance, analysed by Yang *et al.* (1993) and Feng & Leal (1993) with regard to gas bubbles.

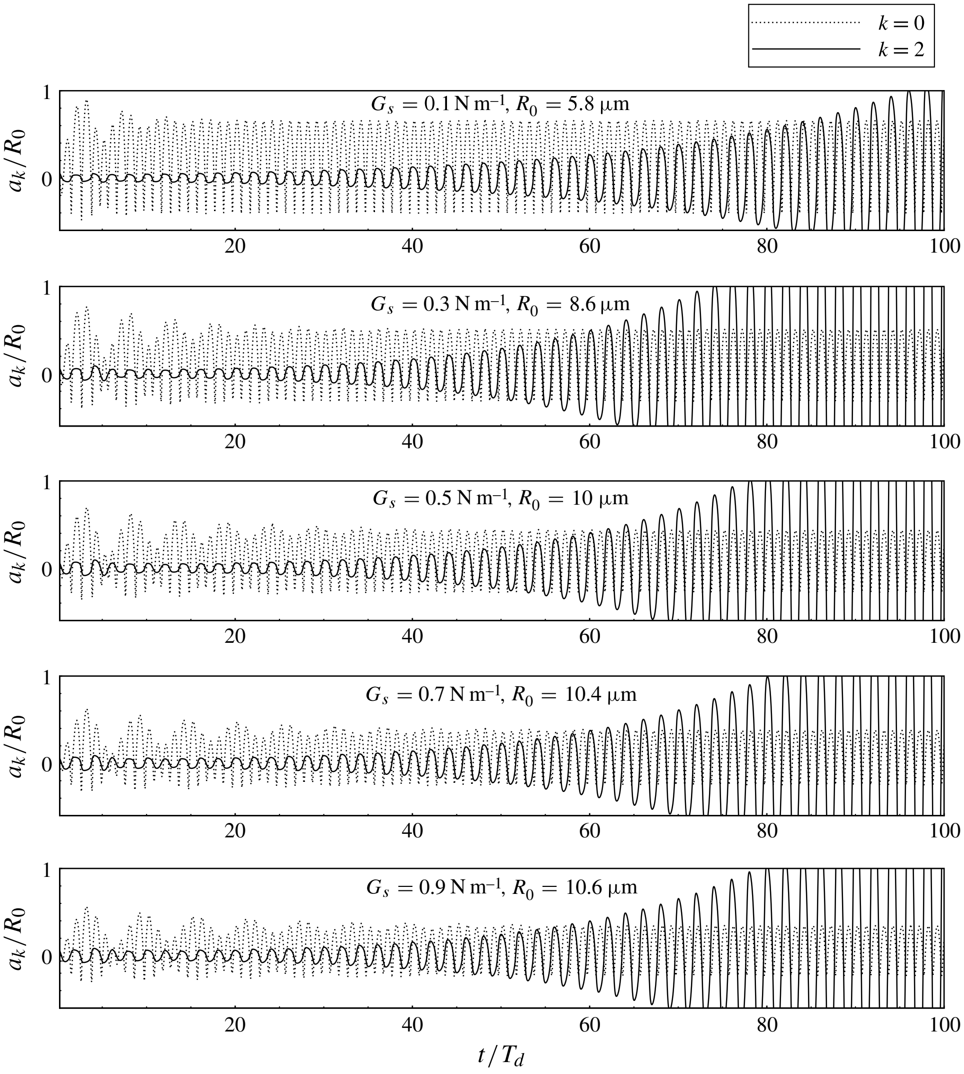

FIGURE 3. Developments of a_0 (dotted line) and a_2 (solid line) with respect to the cases shown in table 1. The time is normalized by the driving period T_d.

Further investigations of the third- and fourth-order shape modes for the case of $G_s = 0.5$ N m, $R_0 = 10$ μm are illustrated in figure 6, together with the second-order shape mode discussed earlier. The natural frequencies for various shape modes are listed in table 2. As shown in figure 6, there are local minima for all three modes in the neighbourhood of $\omega_d/\omega_k = 1$, which can be regarded as direct induction by the driving pressure when its frequency meets the specific higher-order natural frequency. Unlike the second-order mode, for which the one–two resonance is the most unstable situation, the minimum of the curve of $k = 4$ occurs around $\omega_d/\omega_k = 1$. Referring to the ratios of ω_0 and ω_k as shown in table 2 ($\omega_0/\omega_4 = 0.95$), we know that the driving frequency approximates the zeroth-order natural frequency for this minimum, under which the resonance of radial oscillation happens. Looking back to the one–two

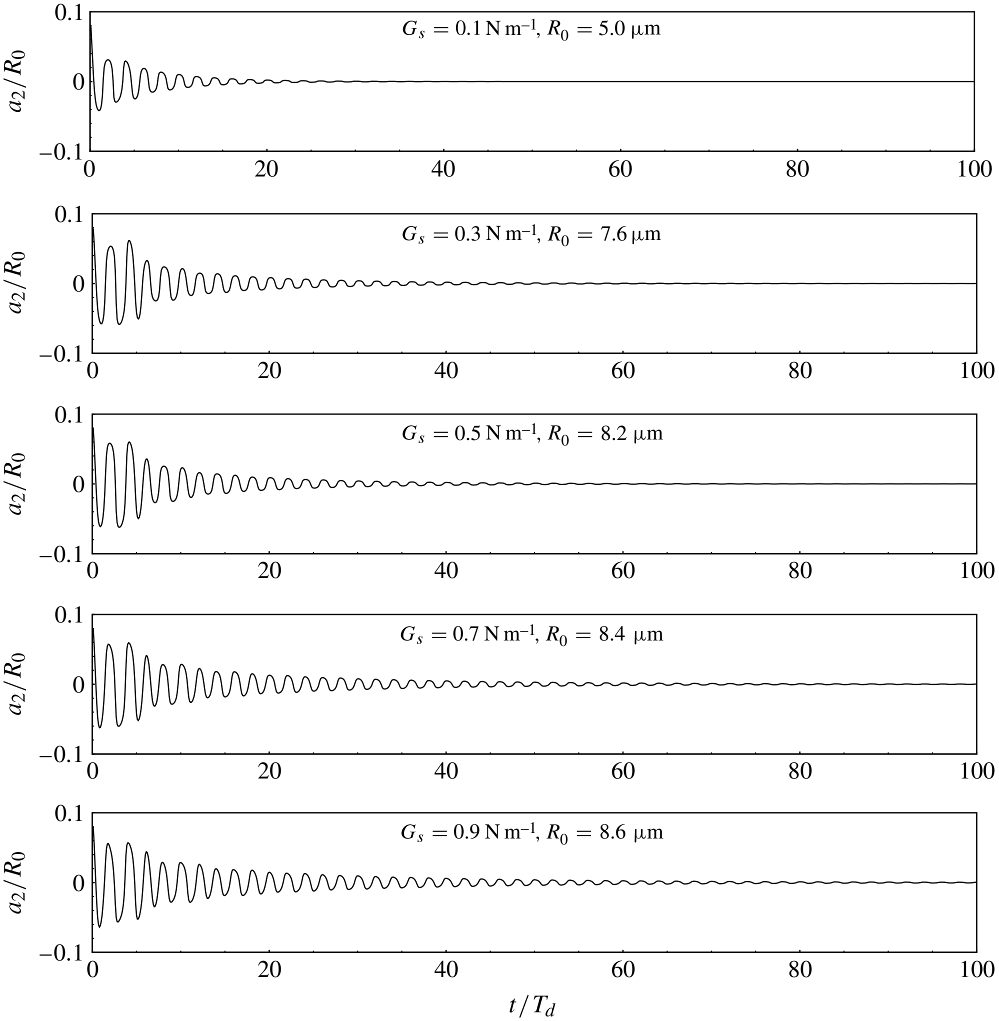

FIGURE 4. Developments of a_2 with respect to the cases with smaller radius than those shown in table 1. The time is normalized by the driving period T_d.

resonance in $k = 2$ and referring to $\omega_0/\omega_2 = 1.66$ in table 2, we also recognize that the minimum in the curve of $k = 2$ satisfies the radial resonance condition. Moreover, for $k = 3$, we can see an obvious decrease in driving amplitude near $\omega_d/\omega_k = 1.2$, which can be considered as the effect of radial resonance as well, since $\omega_0/\omega_3 = 1.24$ (table 2). The above findings allow us to conclude that the shape instability yields preferentially when the bubble is at its radial resonance, which has been found by Dollet *et al.* (2008) in their experiment. Furthermore, we see that the local minima occur when the driving frequency and the natural frequency are integer multiples ($\omega_d/\omega_k = 1, 2, 3, \ldots$). This phenomenon is most pronounced for the fourth-order mode, probably because its zeroth-order and fourth-order natural frequencies happen to be nearly equal.

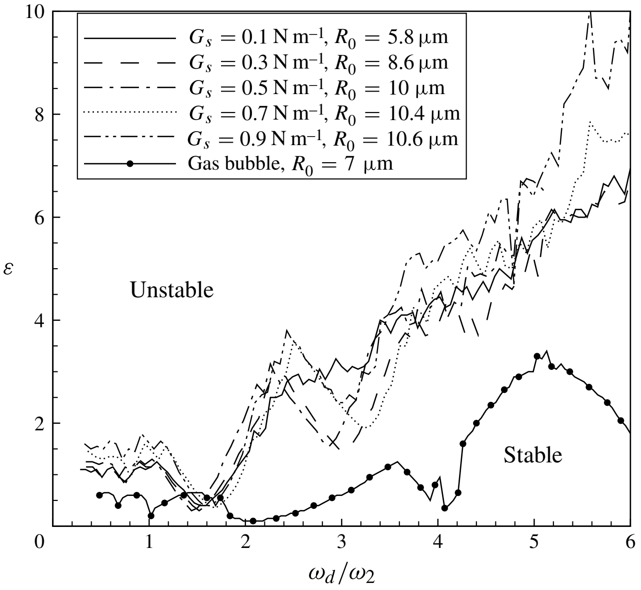

FIGURE 5. Stability diagram of second-order shape mode with respect to the cases shown in table 1 and the case of a gas bubble.

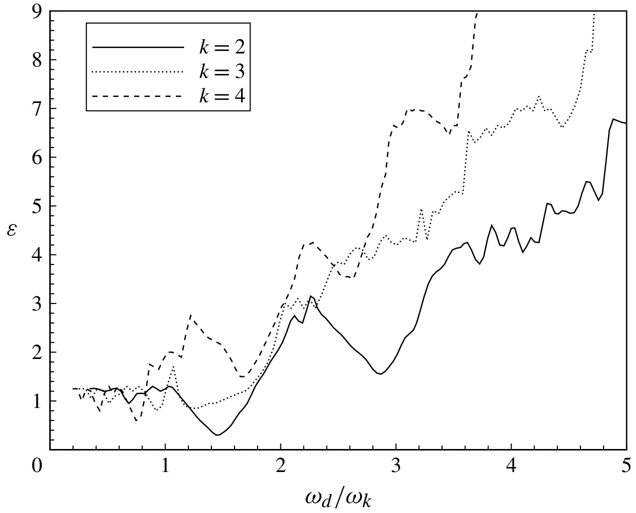

FIGURE 6. Stability diagram of second-, third- and fourth-order shape modes with respect to the case of $R_0 = 10\,\mu\mathrm{m}$, $G_s = 0.5\,\mathrm{N\,m^{-1}}$.

4.2. *Effects of viscosity*

In § 3, in the derivation of the expression for the natural frequency of the higher-order shape mode, we neglected temporal variation of the radial mode, i.e. we assumed that $R = R_0$, $\dot{R} = \ddot{R} = 0$. Consequently, most of the terms with respect to the viscosity were neglected. Although the viscosity has little influence on the natural frequency, which is also recognized in Tsiglifis & Pelekasis (2011), it will affect the system stability. The

k	0	2	3	4
ω_k $(2\pi \times 10^6$ Hz)	0.49	0.29	0.39	0.43
ω_0/ω_k	1	1.66	1.24	0.95
$2\omega_k/\omega_0$	2	1.21	1.61	2.10

TABLE 2. Natural frequencies of various order modes for $G_s = 0.5$ N m^{-1}, $R_0 = 10$ μm.

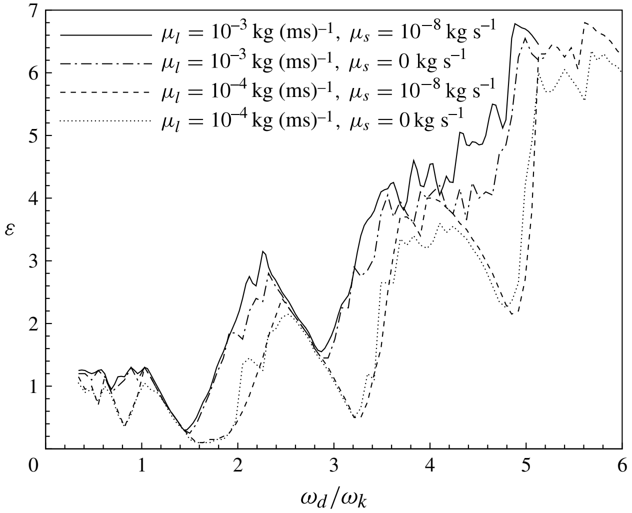

FIGURE 7. Stability diagram of $R_0 = 10$ μm, $G_s = 0.5$ N m^{-1} with various liquid and membrane viscosities.

viscous effect accounts for the damping in the system. It is the competition between the mechanisms to augment and to damp the amplitude that determines the stability of the system. In addition, when the encapsulated bubble is exposed in an ultrasound field, the oscillatory amplitude of the radial mode is non-zero, and so is the radial velocity. Under large pressure driving, the radial oscillation is nonlinear, with slow expansion and sharp contraction (see figure 3). The maximum radial velocity is around 10–20 m s^{-1}. Under this situation, referring to (3.4) and (3.5) and their coefficients (3.6)–(3.13), the magnitude of the terms including $\mu_l\dot{R}/\chi$ becomes comparable with the membrane stress. Figure 7 compares the stability curves under different viscosities. The cases with larger liquid viscosity ($\mu_l = 10^{-3}$ kg (ms)$^{-1}$) are obviously more stable than those with smaller liquid viscosity ($\mu_l = 10^{-4}$ kg (ms)$^{-1}$). By contrast, the effect of membrane viscosity is insignificant. The encapsulating membranes with and without membrane viscosity only differ slightly in stability. The reason is that the membrane viscosity here is a surface viscosity, evaluated by the volumetric viscosity multiplied by the membrane thickness. When the thickness is infinitesimal, the role of membrane viscosity becomes negligible.

5. Summary and conclusions

In this paper, we have derived the equations for the shape oscillation of an encapsulated bubble. The membrane stress, bending moment and viscosity are coupled into the traction jump condition at the bubble surface. Due to the no-slip condition at the membrane, the movement of the material points along the surface, as well as their surface-normal motion, is considered. The non-spherical shape instability is investigated in the context of a viscous incompressible fluid. The derived system bears the structure of Mathieu's equation, which predicts the stability condition of $2\omega_k/\omega_d = n$, where n is an integer. The stability diagrams of the higher-order shape modes validate the unstable condition, and also reveal the important role of liquid viscosity on the system stability.

Acknowledgements

We thank H. Huang and P. Zhang for fruitful discussion. This work was supported by the the Japanese Government Scholarship (No. 073138) of the Ministry of Education, Culture, Sports, Science and Technology (MEXT) and by the Grant-in-Aid for Young Scientists (B) (No. 21760120) of MEXT.

Appendix A. Derivation of velocity and pressure fields

For the decomposed velocity and pressure components in (2.16)–(2.17), following Prosperetti (1977), the governing equations and the boundary conditions are summarized below.

For $(\boldsymbol{u}_0, p_0)$:

$$\nabla \cdot \boldsymbol{u}_0 = 0, \tag{A 1}$$

$$\rho \frac{\partial \boldsymbol{u}_0}{\partial t} + \rho(\boldsymbol{u}_0 \cdot \nabla)\boldsymbol{u}_0 + \nabla p_0 = 0, \tag{A 2}$$

$$\boldsymbol{u}_0 \cdot \boldsymbol{e}_r = \dot{R} \quad \text{at } r = R, \tag{A 3}$$

$$\boldsymbol{u}_0 \to 0, \quad p_0 \to p_\infty \quad \text{as } r \to \infty. \tag{A 4}$$

For $(\boldsymbol{u}_p, p_p)$:

$$\nabla \cdot \boldsymbol{u}_p = 0, \tag{A 5}$$

$$\rho \frac{\partial \boldsymbol{u}_p}{\partial t} + \rho(\boldsymbol{u}_0 \cdot \nabla)\boldsymbol{u}_p + \rho(\boldsymbol{u}_p \cdot \nabla)\boldsymbol{u}_0 + \nabla p_p = 0, \tag{A 6}$$

$$O(\delta) \text{ component of } \frac{\partial S}{\partial t} + (\boldsymbol{u}_0 + \delta \boldsymbol{u}_p) \cdot \boldsymbol{e}_r \frac{\partial S}{\partial r} = 0 \quad \text{at } S = 0, \tag{A 7}$$

$$\boldsymbol{u}_p \to 0, \quad p_p \to 0 \quad \text{as } r \to \infty. \tag{A 8}$$

For $(\boldsymbol{u}_v, p_v)$:

$$\nabla \cdot \boldsymbol{u}_v = 0, \tag{A 9}$$

$$\rho \frac{\partial \boldsymbol{u}_v}{\partial t} + \rho(\boldsymbol{u}_0 \cdot \nabla)\boldsymbol{u}_v + \rho(\boldsymbol{u}_v \cdot \nabla)\boldsymbol{u}_0 + \nabla p_v = \mu_l \nabla^2 \boldsymbol{u}_v, \tag{A 10}$$

$$\boldsymbol{u}_v \cdot \boldsymbol{e}_r = 0 \quad \text{at } r = R, \tag{A 11}$$

$$\boldsymbol{u}_v \to 0, \quad p_v \to 0 \quad \text{as } r \to \infty. \tag{A 12}$$

Note that in addition to the kinematic condition (A 11), the dynamic (2.65) and no-velocity-jump (2.68) conditions on the surface $r = R$ are needed to identity the $(\boldsymbol{u}_v, p_v)$ field.

Considering that the incompressible velocity vectors $\boldsymbol{u}_0$ and $\boldsymbol{u}_p$ are irrotational, and therefore the velocity potentials for them are harmonic, we obtain the velocity vectors (2.22) and (2.23) and the pressures (2.25) and (2.26). For the viscous correction $(\boldsymbol{u}_v, p_v)$, taking the curl of both sides, (A 10) becomes

$$\rho\left(\frac{\partial \boldsymbol{\omega}}{\partial t} + \boldsymbol{\nabla} \times (\boldsymbol{\omega} \times \boldsymbol{u}_0)\right) = -\mu_l \boldsymbol{\nabla} \times (\boldsymbol{\nabla} \times \boldsymbol{\omega}), \tag{A 13}$$

where $\boldsymbol{\omega}(= \boldsymbol{\nabla} \times \boldsymbol{u}_v)$ denotes the vorticity vector. Since the system treated in the paper is axisymmetric, the vorticity vector field due to the k-th order deformation corresponds to a toroidal vector one, namely

$$\boldsymbol{\omega} = \boldsymbol{\nabla} \times (T(r, t)P_k(\cos\theta)\boldsymbol{e}_r), \tag{A 14}$$

where T yields (2.30). The term $\boldsymbol{u}_v$ is written in the form of (2.24) involving a function $\varPhi$, which satisfies

$$\nabla^2 \varPhi = \boldsymbol{\nabla} \cdot (TP_k(\cos\theta)\boldsymbol{e}_r). \tag{A 15}$$

As derived by Prosperetti (1977), the solution to (A 15) is given by (2.28), and the condition of regularity for the velocity at infinity determines (2.29). Integrating (A 10) and eliminating $\partial T/\partial t$ by (2.30) yields the pressure (2.27).

Appendix B. Numerical solution of toroidal field $T(r, t)$

The toroidal field $T(r, t)$ obeys (2.30), which is computed using the finite differential method. We use a transformation so that (2.30) has a fixed computational domain. Letting $y = r/R(t)$ and $\tau = t$, (2.30) becomes

$$\frac{\partial T}{\partial \tau} - \frac{\mu_l}{\rho R^2}\frac{\partial^2 T}{\partial y^2} - \frac{\dot{R}}{R}(y - y^{-2})\frac{\partial T}{\partial y} + \left[\frac{\mu_l k(k+1)}{\rho R^2 y^2} - \frac{2\dot{R}}{y^3 R}\right] T = 0. \tag{B 1}$$

The convection term is discretized by a first-order upwinding scheme, and the diffusion term by a second-order central scheme. Since $y \geqslant 1$, the sign of the coefficient before the convection term is determined by the sign of $\dot{R}$. Equation (B 1) is written in a discretized form:

$$\begin{aligned}\frac{T_i - T_i^{t-1}}{\Delta t} &- \left[\frac{\mu_l}{\rho R^2} + \frac{|\dot{R}|(y - y^{-2})\Delta y}{2R}\right]\frac{T_{i+1} - 2T_i + T_{i-1}}{\Delta y^2} \\ &- \frac{\dot{R}(y - y^{-2})}{R}\frac{T_{i+1} - T_{i-1}}{2\Delta y} + \left[\frac{\mu_l k(k+1)}{\rho R^2 y^2} - \frac{2\dot{R}}{y^3 R}\right] T_i = 0,\end{aligned} \tag{B 2}$$

where the term $|\dot{R}|(y - y^{-2})\Delta y/2R$ comes from the numerical diffusion related to the upwinding scheme for the convection term. The boundary condition of (B 2) at the bubble surface is given by the tangential balance condition (2.65). At infinity, T approaches zero.

The numerical settings are as follows (Ferziger & Perić 2002). The computational domain is set to be $1 \leqslant y \leqslant 2$ to ensure that the boundary of the far field is outside the boundary layer. The grid resolution is 1/100, with grid points uniformly distributed along the y-direction so that the cell Reynolds number is approximately 1. The time step is set as 10^{-4} of the period to satisfy the Courant–Friedrichs–Lewy (CFL) condition.

REFERENCES

An, Y., Lu, T. & Yang, B. 2005 Instability of sonoluminescing bubbles under a nonspherical symmetrical acoustic-pressure perturbation. *Phys. Rev.* E **71** (2), 26310.

Barthès-Biesel, D. 1980 Motion of a spherical microcapsule freely suspended in a linear shear flow. *J. Fluid Mech.* **100**, 931–953.

Barthès-Biesel, D. & Rallison, J. M. 1981 The time-dependent deformation of a capsule freely suspended in a linear shear flow. *J. Fluid Mech.* **113**, 251–267.

Barthès-Biesel, D. & Sgaier, H. 1985 Role of membrane viscosity in the orientation and deformation of a spherical capsule suspended in shear flow. *J. Fluid Mech.* **160**, 119–135.

Bender, C. M. & Orszag, S. A. 1978 *Advanced Mathematical Methods for Scientists and Engineers*. McGraw-Hill.

Benjamin, T. B. 1964 Surface effects in non-spherical motions of small cavities. In *Cavitation in Real Liquids*, pp. 164–180. Elsevier.

Brenner, M. P., Hilgenfeldt, S. & Lohse, D. 2002 Single-bubble sonoluminescence. *Rev. Mod. Phys.* **74** (2), 425–484.

Brenner, M. P., Lohse, D. & Dupont, T. F. 1995 Bubble shape oscillations and the onset of sonoluminescence. *Phys. Rev. Lett.* **75** (5), 954–957.

Chapman, R. B. & Plesset, M. S. 1971 Thermal effects in the free oscillations of gas bubbles. *ASME J. Basic Engng* **93**, 373–376.

Chomas, J. E., Dayton, P. A., May, D., Allen, J., Klibanov, A. & Ferrara, K. 2000 Optical observation of contrast agent destruction. *Appl. Phys. Lett.* **77**, 1056–1058.

Church, C. C. 1995 The effects of an elastic solid surface layer on the radial pulsations of gas bubbles. *J. Acoust. Soc. Am.* **97**, 1510–1521.

Diaz, A., Pelekasis, N. & Barthès-Biesel, D. 2000 Transient response of a capsule subjected to varying flow conditions: effect of internal fluid viscosity and membrane elasticity. *Phys. Fluids* **12**, 948–957.

Dollet, B., van der Meer, S. M., Garbin, V., de Jong, N., Lohse, D. & Versluis, M. 2008 Nonspherical oscillations of ultrasound contrast agent microbubbles. *Ultrasound Med. Biol.* **34** (9), 1465–1473.

Feng, Z. C. & Leal, L. G. 1993 On energy transfer in resonant bubble oscillations. *Phys. Fluids* A **5**, 826–836.

Feng, Z. C. & Leal, L. G. 1997 Nonlinear bubble dynamics. *Annu. Rev. Fluid Mech.* **29** (1), 201–243.

Ferziger, J. H. & Perić, M. 2002 *Computational Methods for Fluid Dynamics*. Springer.

Green, A. E. & Adkins, J. E. 1960 *Large Elastic Deformations and Non-Linear Continuum Mechanics*. Clarendon Press Oxford.

Hao, Y. & Prosperetti, A. 1999 The effect of viscosity on the spherical stability of oscillating gas bubbles. *Phys. Fluids* **11**, 1309–1317.

Hilgenfeldt, S., Lohse, D. & Brenner, M. P. 1996 Phase diagrams for sonoluminescing bubbles. *Phys. Fluids* **21**, 2808–2826.

Hoff, L. 2001 *Acoustic Characterization of Contrast Agents for Medical Ultrasound Imaging*. Springer.

Hoff, L., Sontum, P. C. & Hovem, J. M. 2000 Oscillations of polymeric microbubbles: effect of the encapsulating shell. *J. Acoust. Soc. Am.* **107**, 2272–2280.

Holzapfel, G. A. 2000 *Nonlinear Solid Mechanics: A Continuum Approach for Engineering*. Wiley.

Holzfuss, J. 2008 Surface-wave instabilities, period doubling, and an approximate universal boundary of bubble stability at the upper threshold of sonoluminescence. *Phys. Rev.* E **77** (6), 66309.

de Jong, N., Cornet, R. & Lancée, C. T. 1994 Higher harmonics of vibrating gas-filled microspheres. Part I. Simulations. *Ultrasonics* **32** (6), 447–453.

Khismatullin, D. B. 2004 Resonance frequency of microbubbles: effect of viscosity. *J. Acoust. Soc. Am.* **116**, 1463–1473.

KVIKLIENĖ, A., JURKONIS, R., RESSNER, M., HOFF, L., JANSSON, T., JANEROT-SJÖBERG, B., LUKOSEVICIUS, A. & ASK, P. 2004 Modelling of nonlinear effects and the response of ultrasound contrast micro bubbles: simulation and experiment. *Ultrasonics* **42** (1–9), 301–307.

LAC, E., BARTHES-BIESEL, D., PELEKASIS, N. A. & TSAMOPOULOS, J. 2004 Spherical capsules in three-dimensional unbounded Stokes flows: effect of the membrane constitutive law and onset of buckling. *J. Fluid Mech.* **516**, 303–334.

LAMB, H. 1932 *Hydrodynamics*. Cambridge University Press.

LEYRAT-MAURIN, A. & BARTHES-BIESEL, D. 1994 Motion of a deformable capsule through a hyperbolic constriction. *J. Fluid Mech.* **279**, 135–163.

LI, X. Z., BARTHÈS-BIESEL, D. & HELMY, A. 1988 Large deformations and burst of a capsule freely suspended in an elongational flow. *J. Fluid Mech.* **187**, 179–196.

LINDNER, J. R. 2004 Microbubbles in medical imaging: current applications and future directions. *Nat. Rev. Drug Discov.* **3** (6), 527–533.

LIU, Y., SUGIYAMA, K., TAKAGI, S. & MATSUMOTO, Y. 2011 Numerical study on the shape oscillation of an encapsulated microbubble in ultrasound field. *Phys. Fluids* **23**, 041904.

LOVE, A. E. H. 1888 The small free vibrations and deformation of a thin elastic shell. *Phil. Trans. R. Soc. Lond.* A **179**, 491–546.

MARMOTTANT, P., VAN DER MEER, S., EMMER, M., VERSLUIS, M., DE JONG, N., HILGENFELDT, S. & LOHSE, D. 2005 A model for large amplitude oscillations of coated bubbles accounting for buckling and rupture. *J. Acoust. Soc. Am.* **118**, 3499–3505.

VAN DER MEER, S. M., DOLLET, B., VOORMOLEN, M. M., CHIN, C. T., BOUAKAZ, A., DE JONG, N., VERSLUIS, M. & LOHSE, D. 2007 Microbubble spectroscopy of ultrasound contrast agents. *J. Acoust. Soc. Am.* **121**, 648–656.

MOONEY, M. 1940 A theory of large elastic deformation. *J. Appl. Phys.* **11**, 582–592.

OVERVELDE, M., GARBIN, V., SIJL, J., DOLLET, B., DE JONG, N., LOHSE, D. & VERSLUIS, M. 2010 Nonlinear shell behaviour of phospholipid-coated microbubbles. *Ultrasound Med. Biol.* **36** (12), 2080–2092.

PLESSET, M. S. 1954 On the stability of fluid flows with spherical symmetry. *J. Appl. Phys.* **25** (1), 96–98.

PLESSET, M. S. & PROSPERETTI, A. 1977 Bubble dynamics and cavitation. *Annu. Rev. Fluid Mech.* **9** (1), 145–185.

POSTEMA, M., VAN WAMEL, A., LANCÉE, C. T. & DE JONG, N. 2004 Ultrasound-induced encapsulated microbubble phenomena. *Ultrasound Med. Biol.* **30** (6), 827–840.

POZRIKIDIS, C. 1990 The axisymmetric deformation of a red blood cell in uniaxial straining stokes flow. *J. Fluid Mech.* **216** (-1), 231–254.

POZRIKIDIS, C. 2001 Effect of membrane bending stiffness on the deformation of capsules in simple shear flow. *J. Fluid Mech.* **440** (-1), 269–291.

POZRIKIDIS, C. 2003*a* Deformed shapes of axisymmetric capsules enclosed by elastic membranes. *J. Engng Maths* **45** (2), 169–182.

POZRIKIDIS, C. 2003*b* Numerical simulation of the flow-induced deformation of red blood cells. *Ann. Biomed. Engng* **31** (10), 1194–1205.

POZRIKIDIS, C. 2005 Axisymmetric motion of a file of red blood cells through capillaries. *Phys. Fluids* **17**, 031503.

PROSPERETTI, A. 1977 Viscous effects on perturbed spherical flows. *Q. Appl. Maths* **34**, 339–352.

PROSPERETTI, A. 1991 The thermal behaviour of oscillating gas bubbles. *J. Fluid Mech.* **222**, 587–616.

QUÉGUINER, C. & BARTHÈS-BIESEL, D. 1997 Axisymmetric motion of capsules through cylindrical channels. *J. Fluid Mech.* **348**, 349–376.

SARKAR, K., SHI, W. T., CHATTERJEE, D. & FORSBERG, F. 2005 Characterization of ultrasound contrast microbubbles using in vitro experiments and viscous and viscoelastic interface models for encapsulation. *J. Acoust. Soc. Am.* **118**, 539–550.

STRIDE, E. 2008 The influence of surface adsorption on microbubble dynamics. *Phil. Trans. R. Soc.* A **366** (1873), 2103–2115.

TAKAHIRA, H., AKAMATSU, T. & FUJIKAWA, S. 1991 Dynamics of two nonspherical bubbles in a viscous liquid. *Trans. JSME* B **57**, 447–455.

Tsiglifis, K. & Pelekasis, N. A. 2008 Nonlinear radial oscillations of encapsulated microbubbles subject to ultrasound: the effect of membrane constitutive law. *J. Acoust. Soc. Am.* **123**, 4059–4070.

Tsiglifis, K. & Pelekasis, N. A. 2011 Parametric stability and dynamic buckling of an encapsulated microbubble subject to acoustic disturbances. *Phys. Fluids* **23**, 012102.

Unger, E. C., Hersh, E., Vannan, M., Matsunaga, T. O. & McCreery, T. 2001 Local drug and gene delivery through microbubbles. *Prog. Cardiovasc. Dis.* **44** (1), 45–54.

Versluis, M., Goertz, D. E., Palanchon, P., Heitman, I. L., van der Meer, S. M., Dollet, B., de Jong, N. & Lohse, D. 2010 Microbubble shape oscillations excited through ultrasonic parametric driving. *Phys. Rev.* E **82** (2), 026321.

Yang, S. M., Feng, Z. C. & Leal, L. G. 1993 Nonlinear effects in the dynamics of shape and volume oscillations for a gas bubble in an external flow. *J. Fluid Mech.* **247**, 417–454.